Pergamon

Int. J. Heat Mass Transfer. Vol. 39, No. 16, pp. 3441–3451, 1996

0017-9310/96 $15.00+0.00

0017-9310(95)00398-3

Numerical and experimental determination of flow structure and heat transfer effects of longitudinal vortices in a channel flow

G. BISWAS,† K. TORII,‡ D. FUJII and K. NISHINO

Department of Mechanical Engineering, Yokohama National University, Tokiwadai 156, Hodogaya, Yokohama 240, Japan

(*Received* 22 *December* 1994 *and in final form* 1 *November* 1995)

Abstract—Longitudinal vortices have enormous utility for flow control. Longitudinal vortices are also capable of producing beneficial effects in transport enhancement. The vortices disrupt the growth of the boundary layer and serve ultimately to bring about enhancement of heat transfer between the fluid and its neighboring surface. The present study determines the flow structure, in detail, behind a winglet type vortex generator placed in a fully developed laminar channel flow. The flow structure is complex and consists of a main vortex, a *corner vortex* and induced vortices. Experiments are performed in order to corroborate the numerical predictions of the flow structure. The purpose of this study is to show the performance of a delta winglet type vortex generator in improving heat transfer. The conclusions that are drawn identify plausible choice regarding the optimal angle of attack of the vortex generator. Such vortex generators show great promise for enhancing the heat transfer rate in plate–fin *crossflow* heat exchangers. Copyright © 1996 Elsevier Science Ltd.

INTRODUCTION

Requirements of small-size and lightweight heat exchanger devices in power, process and aerospace industries have resulted in the development of specially designed heat transfer surfaces [1]. It is possible to distinguish different basic flow configurations, such as internal flow through tubes, external flow normal to the tubes and channel flows in a wide range of heat exchangers. In most practical cases, the heat transfer coefficients for the configuration of flow over flat surfaces are significantly low. In order to enhance heat transfer between the flowing fluid and closely-spaced parallel plate channels, in the case of plate–fin heat exchangers, protrusions can be mounted on the channel surfaces. The protrusions in the form of slender delta wing or winglet-type vortex generators are capable of enhancing heat transfer at the expense of relatively less increase in pressure penalty as compared to other protrusions.

Experimental investigations of Russel *et al.* [2], Fiebig *et al.* [3, 4], Torii *et al.* [5] and Tiggelbeck *et al.*, [6] reveal the enhancement of heat transfer in the presence of longitudinal vortices. The longitudinal vortices are characterized by their rotating motion and longevity. Eibeck and Eaton [7] have conducted experiments on longitudinal vortices embedded in a turbulent boundary layer and observed their influence on heat transfer. Despite the presence of turbulent diffusion, the influence of longitudinal vortices on momentum and energy transport can be traced at a location as far downstream as 60 wing chords behind the delta winglet.

Computational studies on related topics have been performed by Fiebig *et al.* [8] and Biswas and Chattopadhyay [9] in a geometrical configuration of delta wing placed inside a rectangular channel. Both studies confirm significant transport enhancement. In another recent study, Biswas *et al.* [10] have indicated that the winglets are a more attractive choice than delta wings as vortex generators for enhancing heat transfer.

The vortex-wake behind a slender winglet-type obstacle described a complex flow structure. Figure 1 shows a typical wake structure generated by a winglet (see Torii *et al.* [11]). The main vortex is formed by the flow separation at the leading edge of the winglet, while the corner vortex is formed by the deformation of the near wall vortex lines at the pressure side of the winglet. In addition, the presence of induced vortices has also been observed in some cases. Torii *et al.* [11] have accomplished velocity measurements to understand the complex vortical structure of the flow. They have employed a rotation probe technique with a slant hot-wire sensor for the measurement of the velocity components downstream of the vortex generator on a flat plate. However, the channel flows have some different features than the flat-plate boundary-layer flows. A favorable pressure gradient always persists in channel flows and becomes larger with decreasing Reynolds number. Besides, channel flows have a tendency to become fully developed in the downstream.

† On leave from Department of Mechanical Engineering, Indian Institute of Technology, Kanpur (U.P.) 208016, India.

‡ Author to whom correspondence should be addressed.

NOMENCLATURE

B	channel width
b	height of the winglet
C_p	specific heat of the fluid
H	channel height
h	heat transfer coefficient, $-k(\partial T/\partial y)_w/(T_w-T_b)$
j/f	quality factor, equation (7)
k	thermal conductivity of the fluid
Nu	local Nusselt number based on bulk temperature of the fluid, $h(2H)/k$
$\overline{Nu}$	spanwise average Nusselt number
n	iterations in time step
P	nondimensional pressure, $p/\rho U_{av}^2$
Pr	Prandtl number, $\mu C_p/k$
p	pressure
q	wall heat flux
Re	Reynolds number, $U_{av}(2H)/\nu$
S	wing area
s	pitch of winglets
T	temperature
t	time
U	u/U_{av}
u	axial component of velocity
V	v/U_{av}
v	vertical component of velocity
W	w/U_{av}
w	spanwise component of velocity
X	x/H
x	axial dimension of the coordinates
Y	y/H
y	vertical or normal dimension of coordinates
Z	z/H
z	spanwise dimension of coordinates.

Greek symbols

α	aspect ratio of the channel, B/H
β	angle of attack of the winglet
Γ	time period of oscillation
θ	nondimensional temperature, $(T-T_\infty)/(T_w-T_\infty)$
Λ	aspect ratio of the winglet, b^2/S
μ	dynamic viscosity of the fluid
ν	kinematic viscosity of the fluid
τ	nondimensional time
Ω_x	nondimensional vorticity
ω_x	vorticity, $\partial w/\partial y-\partial v/\partial z$.

Subscripts

av	average
b	bulk condition
c	cross-stream plane
r	trailing edge
sa	spanwise average combination of top and bottom plates
w	wall
1	bottom fin-plate
2	top fin-plate
∞	inlet condition.

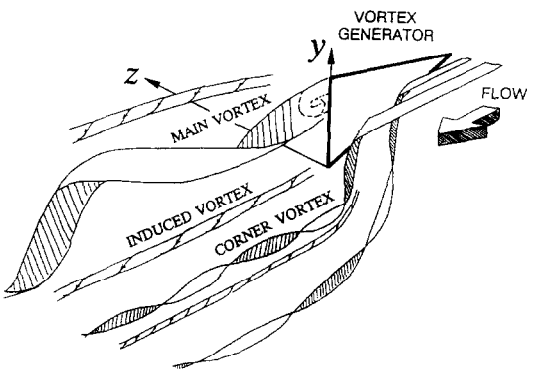

Fig. 1. The wake structure generated by a winglet.

The present study is aimed at a numerical investigation of flow structure and heat transfer in a channel with a built-in winglet type vortex generator placed in a fully developed laminar flow. The study also has the following purposes:

(1) comparison of the predicted flow structure with the experimentally obtained flow structure measured by a hot-wire-anemometer;

(2) prediction of heat transfer and pressure drop characteristics for different geometrical parameters.

STATEMENT OF THE PROBLEM

Computation is performed in a channel which is formed by two neighboring fins (Fig. 2). An obstacle in the form of a winglet is placed inside. One side of the winglet is fixed on the bottom wall and the trailing-edge is free. The height of the winglet is b and the angle of attack is β. The aspect of ratio of the winglet is Λ $(=b^2/S)$. The dimensionless equations for continuity, momentum and energy for this problem may be expressed in their conservative form as

$$\frac{\partial U_i}{\partial X_i} = 0 \tag{1}$$

$$\frac{\partial U_i}{\partial \tau} + \frac{\partial}{\partial X_j}(U_i U_j) = -\frac{\partial P}{\partial X_i} + \frac{1}{(Re/2)}\left[\frac{\partial}{\partial X_j}\left(\frac{\partial U_i}{\partial X_j} + \frac{\partial U_j}{\partial X_i}\right)\right] \tag{2}$$

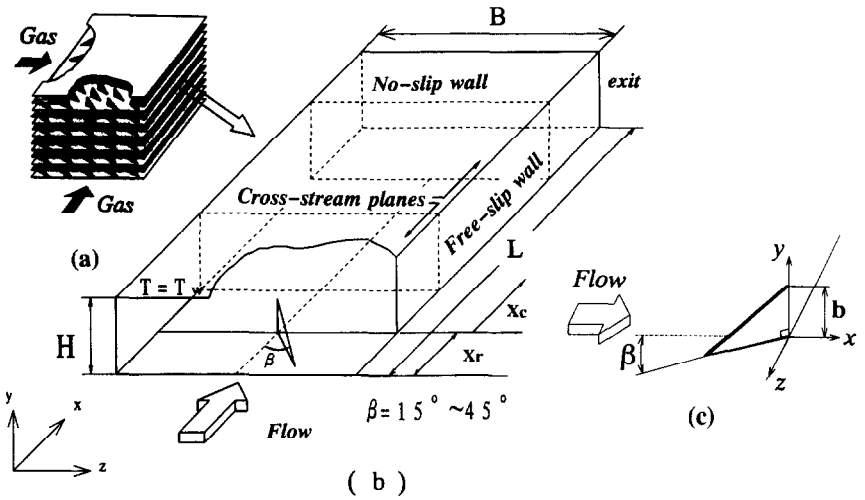

Fig. 2. (a) Proposed surface geometry for the heat exchange, (b) flow model for simulation, (c) main flow and the winglet.

$$\frac{\partial\theta}{\partial\tau}+\frac{\partial}{\partial X_j}(\theta U_j)=\frac{1}{(Re/2)\cdot Pr}\cdot\frac{\partial}{\partial X_j}\left[\frac{\partial\theta}{\partial X_j}\right]. \quad (3)$$

In the above equations, velocities have been non-dimensionalized with the average incoming velocity U_{av} at the channel inlet, all lengths with the height of the channel H, the pressure with ρU_{av}^2, and the non-dimensional temperature is defined as $\theta=(T-T_\infty)/(T_w-T_\infty)$. The Reynolds number is defined on the basis of average axial velocity at the inlet and the characteristic dimension ($2H$) of the channel as $Re=U_{av}(2H)/v$. Boundary conditions of interest in this investigation are

at $Y=0$ and $Y=1$

$$U=V=W=0;\quad \theta=1$$

at $Z=0$ and $z=B/H$

$$W=\left(\frac{\partial V}{\partial Z}\right)=\left(\frac{\partial U}{\partial Z}\right)=\left(\frac{\partial\theta}{\partial Z}\right)=0$$

at $X=0$

$$U=U(Y)\quad V=W=\theta=0$$

at $X=L/H$

$$\frac{\partial^2 U}{\partial X^2}=\frac{\partial^2 V}{\partial X^2}=\frac{\partial^2 W}{\partial X^2}=\frac{\partial^2\theta}{\partial X^2}=0.$$

No-slip conditions for the velocities on the obstacle are used. The temperature of the obstacle is constant and equal to T_w. At the inlet of the channel, a fully developed velocity profile for the axial velocity is used.

METHOD OF SOLUTION

A modified version of the Marker and Cell (MAC) method of Harlow and Welch [12] and Hirt and Cook [13] is used to obtain the numerical solution of equations (1)–(3). The computational domain is divided into a set of Cartesian cells. A staggered grid arrangement is used such that the velocity components are defined at the center of the cell faces to which they are normal. The pressure and temperature are defined at the center of the cell.

Two fold solutions for the velocities are obtained. At any time $(n+1)\Delta\tau$, a provisional velocity field is calculated by using the pressure gradients at $n\Delta\tau$. In the second fold, the pressure field at $(n+1)\Delta\tau$ is calculated by an iterative procedure and the provisional velocity field is corrected to be divergence free. This iterative correction of the velocity field through the implicit continuity equation is equivalent to solution of Poisson's equation for pressure. The process is repeated successively in all cells until a divergence-free velocity field is reached with a prescribed upper bound; here a value of 0.0001 has been chosen. This solution scheme is continued until a steady or periodic flow is obtained. After evaluating the correct velocities, the energy equation is solved with a successive overrelaxation technique to determine the temperature field. The convective terms of Navier–Stokes and energy equations were discretized by a weighted average scheme (Hirt *et al.* [14]). The factor for the upwind contribution was restricted below 0.2 so that the influence of numerical viscosity is small. Admittedly, a more accurate spatial differencing scheme could have been used for the present study. However, in a similar flow configuration, Biswas *et al.* [10] have observed a marginal change in the predicted values over the predictions due to the weighted average scheme by using another scheme having a higher degree of local accuracy. However, in the present simulations very fine grids have been use to offset this limitation.

PERTINENT PERFORMANCE PARAMETERS

In order to have a quantitative estimation of the heat transfer performance, the combined spanwise average Nusselt number

$$\overline{Nu}_{sa} = \frac{B(q_1+q_2)(2H/k)}{\int_0^B (T_{w1}(x,z)-T_b(x))\,dz + \int_0^B (T_{w2}(x,z)-T_b(x))\,dz} \quad (4)$$

has been calculated at each longitudinal location in the channel. The average Nusselt number in a channel from the inlet up to any axial location at the downstream is calculated using the value of combined spanwise average Nusselt number as

$$\overline{Nu}_x = \frac{1}{X}\int_0^x \overline{Nu}_{sa}\,dx. \quad (5)$$

The pressure drop in the channel is evaluated by using the apparent friction factor f_{app} defined by Shah and London [15] as

$$f_{app} = \left(\frac{p_1 - p_2}{\frac{\rho}{2}U_{av}^2}\right)\left(\frac{2H}{\Delta x}\right). \quad (6)$$

In equation (6) the index 1 means inlet, index 2 means any axial location at the downstream and Δx indicates the distance between the locations 1 and 2. The parameter $2H$ is the characteristic dimension (hydraulic diameter) of the channel.

In order to summarize the performance of the winglet type vortex generators, we define a quality factor as the ratio of the mean-Colburn-factor to the apparent friction-factor over a zone from the inlet to any axial location in the channel as

$$\frac{j}{f} = \frac{\overline{Nu}_x/(Re\cdot Pr^{1/3})}{f_{app}/8.0}. \quad (7)$$

The variation of these performance parameters with respect to different input parameters will be discussed in a subsequent section.

SPATIAL GRID INDEPENDENCE

Considerable effort has been devoted to obtain grid independent results. For $Re = 1580$ and $Pr = 0.7$, in a channel ($\alpha = 3$) with a built-in delta winglet ($\Lambda = 0.81$) at an angle of attack (β) of 15°, grid independent behavior was demonstrated by achieving excellent agreement between results obtained for $(90\times22\times97)$ and $(120\times27\times119)$ grids. In the foregoing specification of grids, the numbers in brackets represent grid points in the x, y and z directions, respectively. The distribution of combined spanwise average Nusselt number in the channel for three different grid-meshes, such as (Grid I: $59\times15\times63$), (Grid II: $90\times22\times97$) and (Grid III: $120\times27\times119$), was compared. The maximum discrepancy of the value of combined spanwise average Nusselt number for Grid II and Grid III was found to be below 1.4%. Hence, most computations for a channel with $\alpha = 3$ are performed by using a (22×97) cross-stream ($\equiv y\times z$) grids. For a wider channel ($\alpha = 5$), and a winglet with similar geometrical configuration, a cross-stream grid of (22×159) was found to be grid independent. The grids in the streamwise direction are suitably chosen to cover the length of the channel. The computations were performed on a HP 9000/735crx Workstation.

EXPERIMENTAL METHOD

The experiments are conducted in a rectangular duct which has a cross-section of 0.3 m × 0.02 m and a length of 1.2 m. The duct is attached to a centrifugal blower and the test section is on the suction side of the blower. A parabolic velocity profile with a free-stream turbulence level of 0.6% is ensured at a section upstream of the location of the vortex generator. The average velocity at the inlet is 0.6 m s^{-1} which was kept constant within ±0.4% variation during a measurement run typically for about 24 h.

All three components of the velocity have been measured simultaneously by a rotation probe. The rotation probe technique uses a slant TSI miniature probe (model 1263-T1.5) of 4 μm diameter tungsten wire with 45° inclination angle and 1 mm length. The probe is mounted on a two-dimensional traversing mechanism for multipoint velocity measurement at different cross-stream planes behind the vortex generator. The rotation and traversing mechanisms are fully automated and the system is capable of performing measurement at typically 8000 points on a cross-flow plane. The calibration and measurement procedures of the rotation probe are well documented elsewhere [11, 16].

RESULTS AND DISCUSSION

Computations have been carried out in a channel of length $L/H = 10.4$. The trailing edge of the winglet is located at a distance $X_T = 2.856$ from the inlet. The aspect ratio of the winglet (Λ) is 0.81 and the height of the winglet, b, is equal to channel height H for all the cases. Two different channel aspect ratios (α), viz. $\alpha = 3.0$ and $\alpha = 5.0$ have been chosen for this simulation. Various angles of attack (β) of the vortex generator are used as the governing input parameters. Air has been assumed as a working fluid; hence the Prandtl number of this study is 0.7.

The development of the secondary flow is shown in Fig. 3 for a channel with $\alpha = 3$ and $Re = 1580$. The angle of attack of the vortex generator (β) for this case is 15°. The maximum cross-flow velocity is nearly equal to the mean axial velocity. The elliptic deformation of the vortical structure due to the channel walls becomes obvious when the cross-flow at any two stations downstream of the winglet are compared.

The constant axial velocity lines are shown in Fig. 4 at a cross-section $X_c = 2.5$ behind the trailing edge of winglet of $\Lambda = 0.81$ at $\beta = 15°$ and $Re = 1580$ for

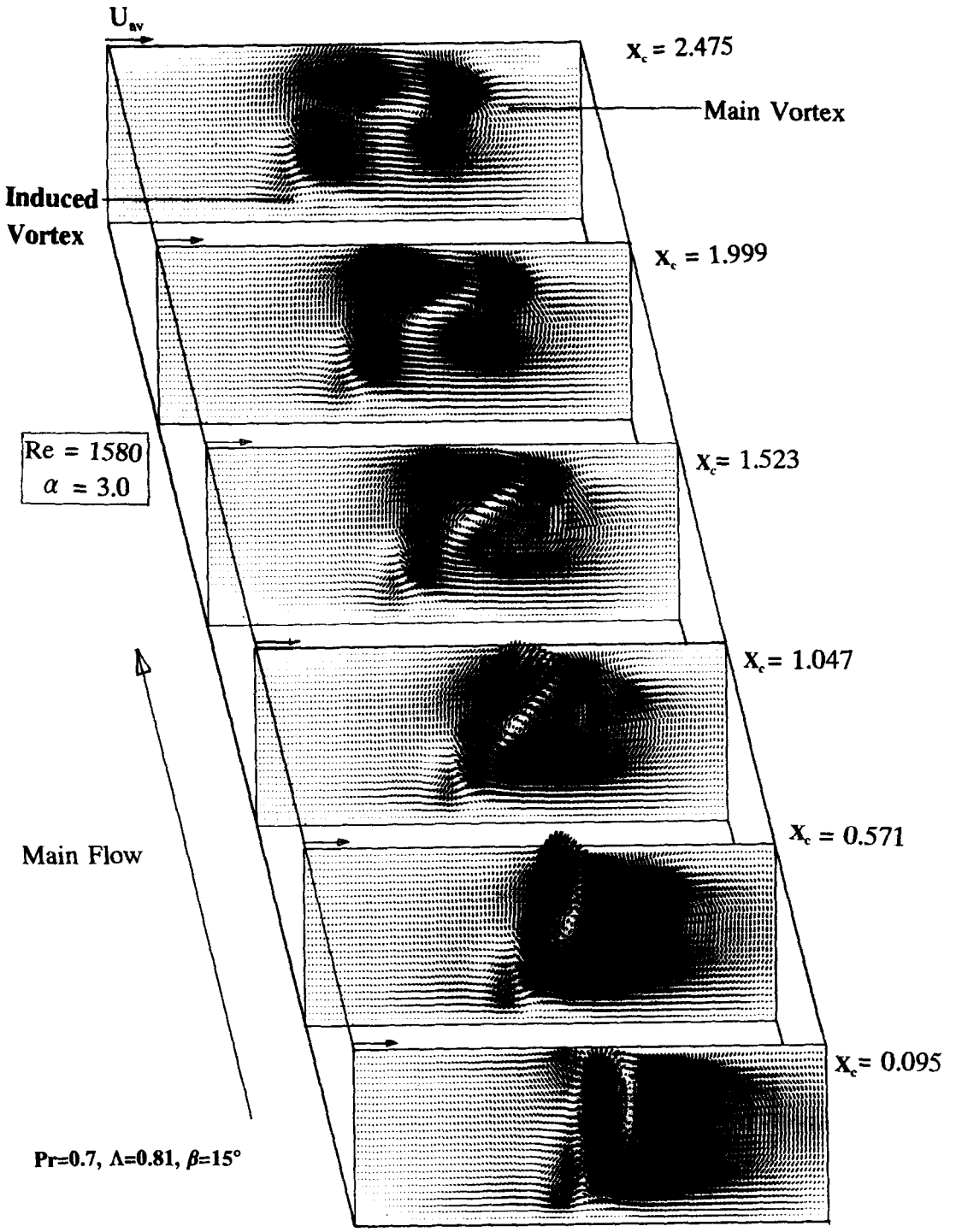

Fig. 3. Formation of vortices behind the winglet in a channel.

$\alpha = 3.0$. The velocity in this plot has been scaled with respect to the maximum axial velocity at the cross-stream plane. The maximum velocity is found to be 1.659 times the average axial velocity at the inlet. Here the vortex axis lies at about the mid-plane of the channel height and the axial velocity has a low value at the axis. It is evident that the computed value of 0.38 for the axial velocity at the vortex axis is indeed very close to the corresponding measured value of 0.39 at the same location.

Figure 5 compares the experimental and computational axial velocity contours in a channel ($\alpha = 5.0$) at a cross-section $X_c = 2.5$ behind the trailing edge of a winglet of $\Lambda = 0.81$ at $\beta = 30°$ and $Re = 1580$. In both the cases, on the bottom plate behind the winglet, the vortices lead to a thinning of

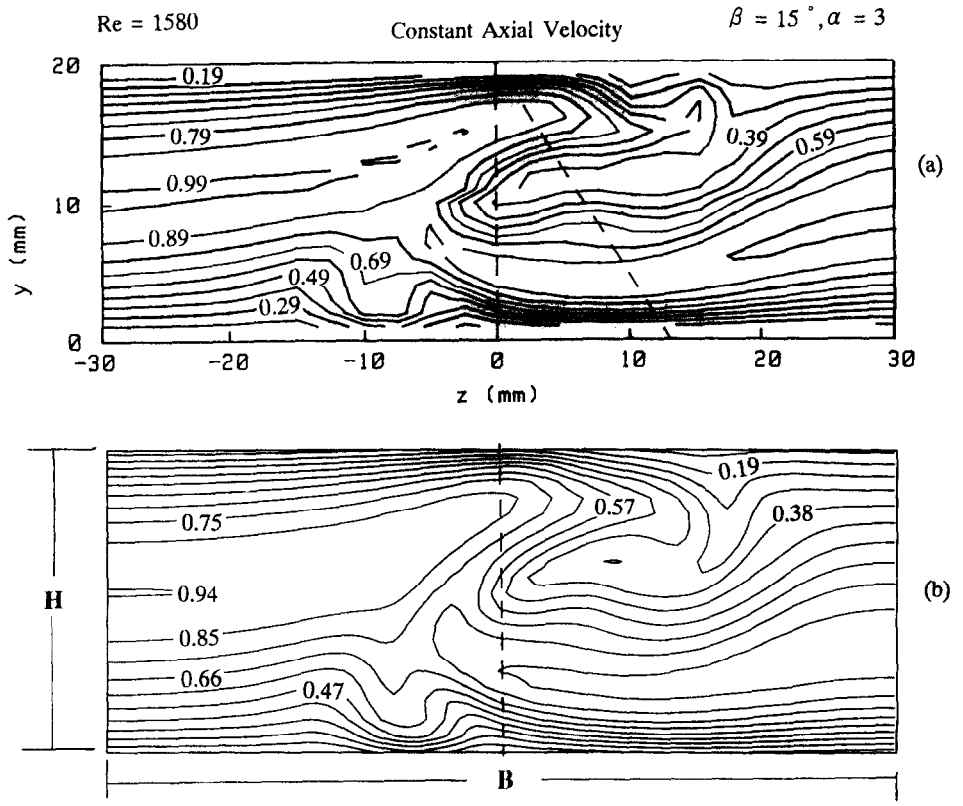

Fig. 4. Constant axial velocity lines at a cross-plane $X_c = 2.5$ behind the winglet at $\beta = 15^\circ$ (a) experiment, (b) computation.

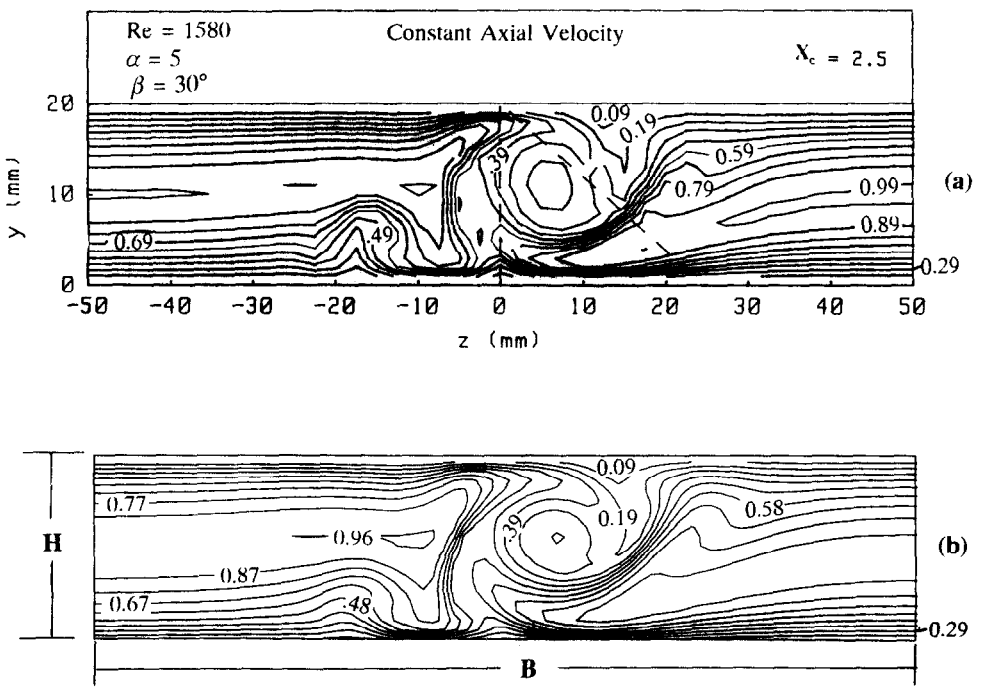

Fig. 5. Constant axial velocity lines at a cross-plane $X_c = 2.5$ behind the winglet at $\beta = 30^\circ$ (a) experiment, (b) computation.

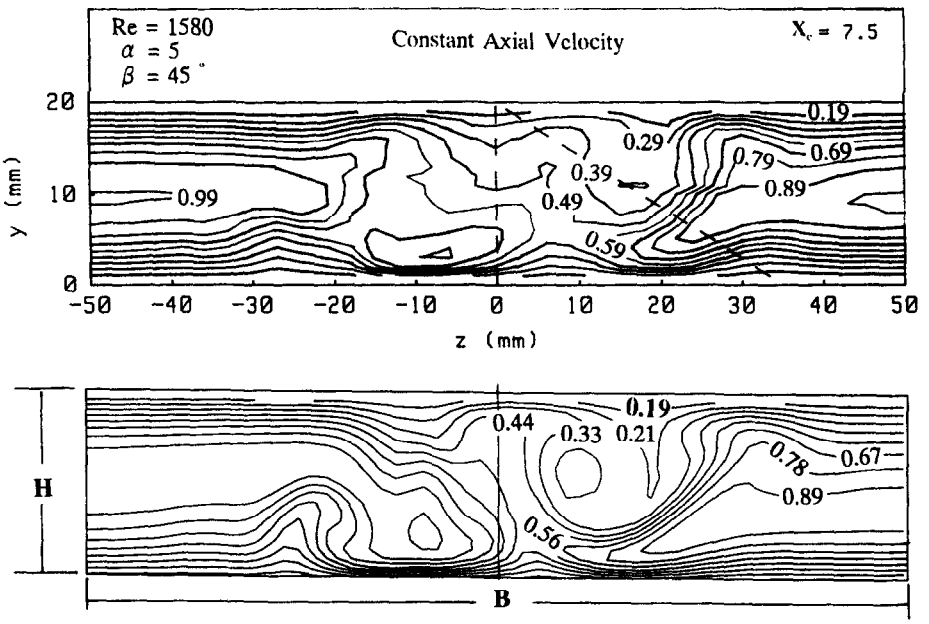

Fig. 6. Constant axial velocity lines at a cross-plane $X_c = 7.5$ behind the winglet at $\beta = 45°$ (a) experiment, (b) computation.

the velocity boundary layer in the downwash region. The thickening of the boundary layers at the array symmetry planes is also evident in both experiment and computation. It may be mentioned that, for the constant axial velocity contours at any section, the velocities are scaled with respect to the maximum axial velocity at that section. In this particular case, the U_{max} is equal to 1.683 times the average axial velocity at the inlet.

At another cross-stream plane ($X_c = 7.5$), the comparison of measured and computed axial velocity contours behind the trailing edge of a winglet of $\Lambda = 0.81$ at $\beta = 45°$ and $Re = 1580$, has been displayed in Fig. 6. All the salient features of the earlier cases are illustrated in this simulation.

In order to understand the vortex structure behind the winglet, the constant vorticity contours for computational and experimental results at a cross-stream plane ($X_c = 2.5$) are compared in Fig. 7. Here, the nondimensional vorticity is defined as

$$\Omega_x = \frac{\omega_x b}{U_{max}} \tag{8a}$$

and ω_x is given by

$$\omega_x = \frac{\partial w}{\partial y} - \frac{\partial v}{\partial z}. \tag{8b}$$

Both the computational and experimental vorticity contours confirm formation of the main vortex, the induced vortices and the corner vortex. The formation of the corner vortex has to be discussed with the help of Fig. 8. As the fluid approaches the stagnation line of an obstacle, it slows down and its pressure increases. The smaller velocity in the boundary layer on the flat bottom wall which is attached to the side of the winglet leads to a smaller pressure increase. Thus, the induced pressure gradient causes a flow towards the bottom wall which interacts with the main-stream. The fluid rolls up forming vortices which are finally swept around the obstacle base and are carried downstream. These vortices are usually known as horseshoe vortices, though looking like a half horseshoe in the present case. Since they are generated at the location of the junction of the winglet and the flat bottom plate, we shall call them corner vortices. The induced vortices (refer to Fig. 7) rotate opposite (counterclockwise) to the main and corner vortices (clockwise). It can be seen that the main vortex axis lies at about the mid-plane in the vertical direction and it is shifted to the right hand side on the y–z plane. The magnitude, direction and location of the constant vorticity contours for the experimental and computational studies agree with each other reasonably well.

It may be mentioned that for the case of flow in a channel ($B/H = 5.0$) with a built-in winglet of $\Lambda = 0.81$ at $\beta = 45°$ and $Re = 1580$, the flow is found to be periodic. In the computational study, we record the velocity components at a location $P(X_c = 2.4, Y = 0.3, Z = 2.5)$ in the channel. The recorded signals of the velocity components in the wake result in sinusoidal waves. To understand the phenomenon further, the phase portrait and power spectra of the signals have been obtained. The phase plane behavior is shown in Fig. 9. The phase portrait shows a limit cycle behavior, and the existence of a single dominant nondimensional frequency ($fr = H/U_{av}\Gamma = 0.3163$) is observed from power spectrum.

Figure 10 shows the longitudinal distribution of the combined spanwise average Nusselt number (com-

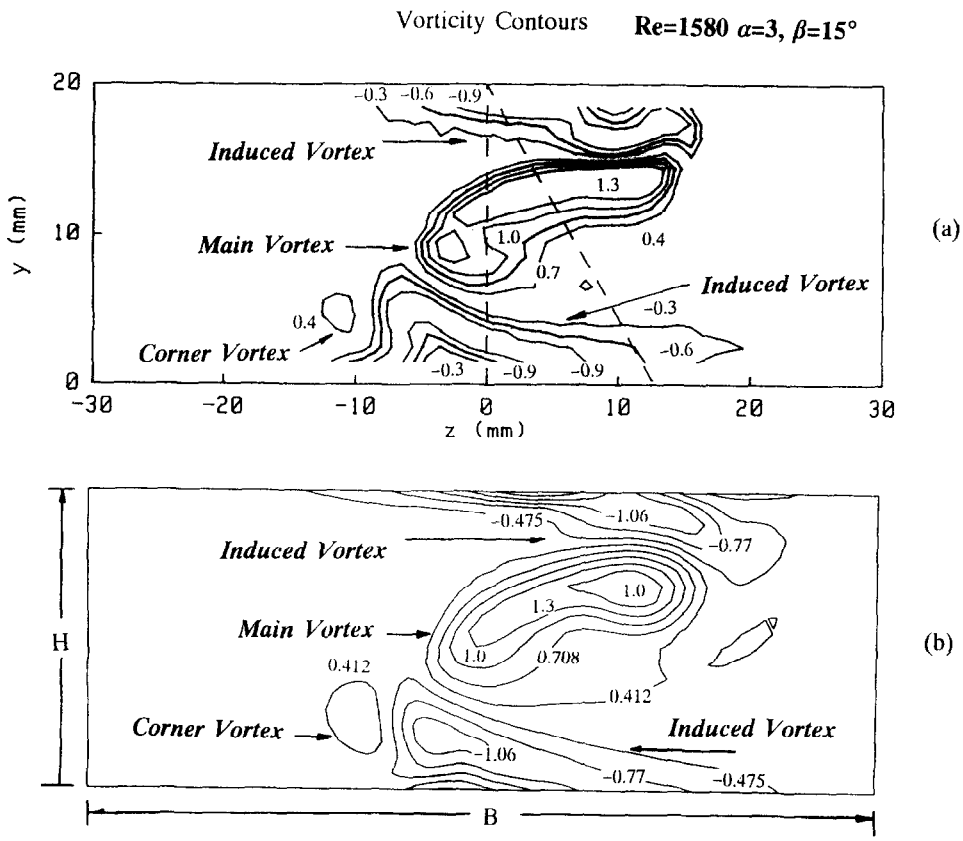

Fig. 7. Vorticity contours behind a cross-plane $X_c = 2.5$ behind the winglet at $\beta = 15°$ (a) experiment, (b) computation.

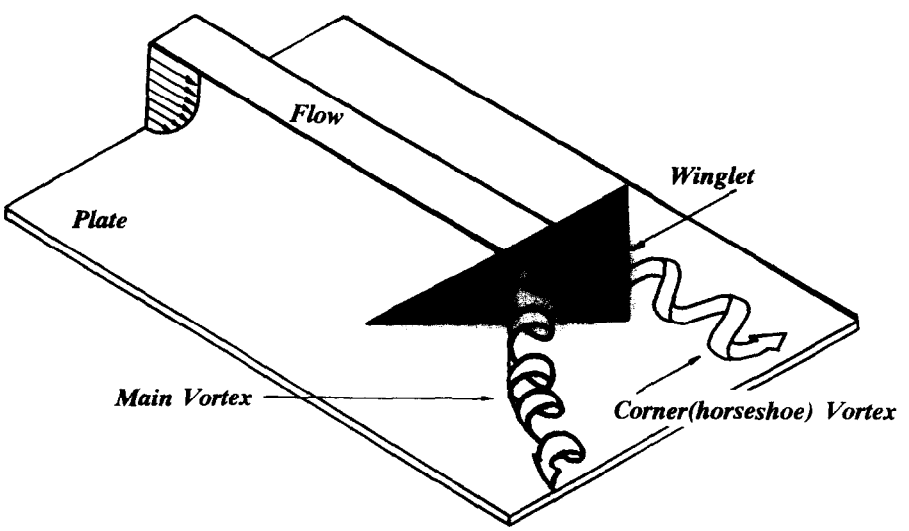

Fig. 8. Formation of a corner vortex due to the winglet.

puted values) in a channel of $\alpha = 3.0$. The combined spanwise average Nusselt number increases with increasing angle of attack. Winglets with higher angle of attack produce vortices with higher strength, which results in a better heat transfer. At a nondimensional axial distance of 2.5 from the trailing edge of the winglet, for an angle of attack of 15°, we observe an enhancement of 32% in $\overline{Nu}_{sa}$ over the case of a plane channel. At the same location, improvements of 48, 57 and 65% in $\overline{Nu}_{sa}$ over the case of a plane channel are observed for $\beta = 22.5°$, 30.0° and 37.5°, respectively.

In order to summarize the performance of the vortex generators, we look at the distribution of (j/f), given by equation (7), in the channel. In Fig. 11, we

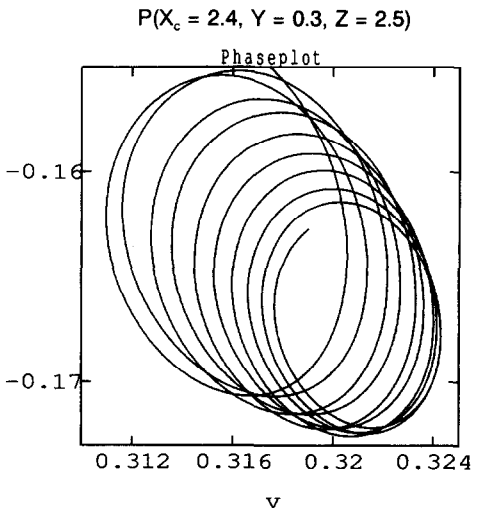

Fig. 9. Phase portrait at a point P in the wake.

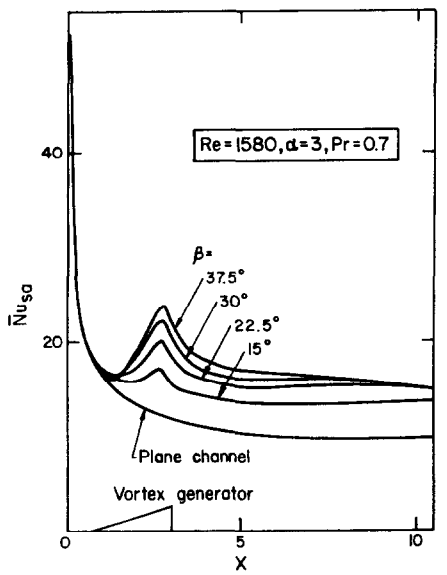

Fig. 10. Effect of angle of attack on the distribution of combined spanwise average Nusselt number in a channel ($\alpha = 3$).

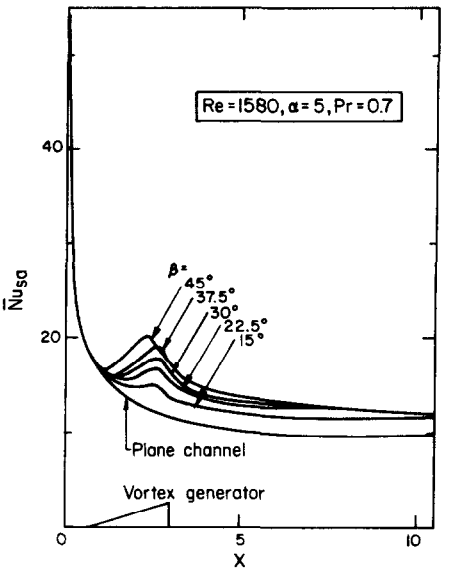

Fig. 12. Effect of angle of attack on the distribution of combined spanwise average Nusselt number in a channel ($\alpha = 5$).

observe a much higher value of (j/f) for $\beta = 15°$ over that of $\beta = 22.5°$, 30° and 37.5° at any axial location in the channel. At the exit of the channel, the (j/f) for $\beta = 15°$ attains a value of 0.88 which is very close to unity. It may be mentioned that the (j/f) values are the results of the computational study.

As we have stated before, the flow configuration closely resembles a single element of a cascade in plate–fin crossflow heat exchangers. The pitch (s) of placing the winglets determines the gap between the array symmetry planes in a channel, which in turn determines the width of the channel. Hence, to know the performance of the winglet type vortex generators in another channel with different aspect ratio ($\alpha = 5$) will be of interest. Figure 12 shows the distribution of combined spanwise average Nusselt number in a channel with $\alpha = 5.0$ for different angles of attack of the vortex generator. As it was seen in the channel

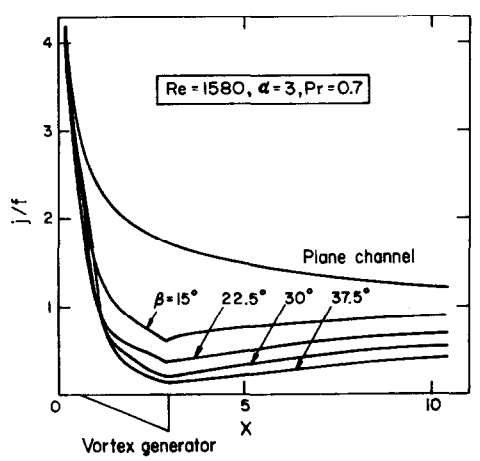

Fig. 11. Distribution of j/f in a channel ($\alpha = 3$) for different angles of attack of the winglet.

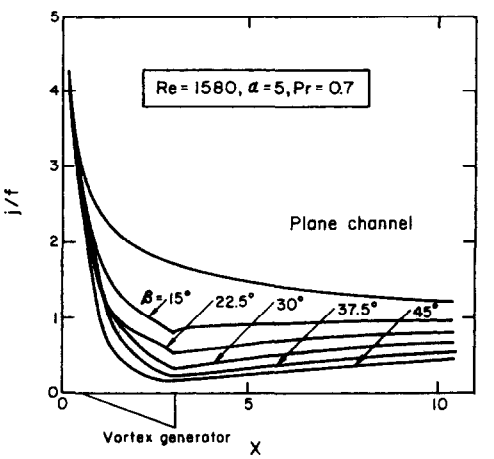

Fig. 13. Distribution of j/f in a channel ($\alpha = 5$) for different angles of attack of the winglet.

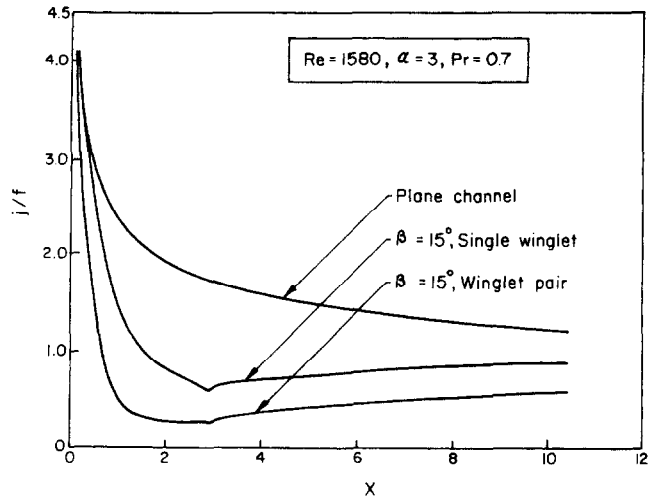

Fig. 14. Distribution of j/f in a channel ($\alpha = 3$) for a single winglet and a winglet pair.

with $\alpha = 3.0$, the winglets with higher angle of attack produce vortices with higher strength, which in turn results in improved heat transfer. However, even for a very long channel ($L/H = 10.4$), the enhancement in heat transfer at the exit of the channel due to the winglet with $\beta = 15^\circ$ is about 19% over the plane channel value. The distribution (j/f) for different values of β of the winglet in a channel of $\alpha = 5.0$ has been shown in Fig. 13. It is evident that the performance of the winglet is best for an angle of attack of 15°. The value of (j/f) for $\beta = 15^\circ$ is 0.95 at the exit of the channel.

Biswas *et al.* [10] have concluded that the winglet pair is a very attractive vortex generator. It is of considerable interest to compare the performance of a winglet pair and single winglet for same angle of attack. Figure 14 shows the j/f distribution in the channel for a winglet pair and a single winglet for an angle of attack of 15°. The comparison shows better performance for a single delta winglet.

CONCLUSION

A delta winglet generates a complex system of longitudinal vortices behind it. The main vortex is formed by the flow separation at the leading edge of the winglet, while the corner vortex has a horseshoe vortex-like characteristic feature. The induced vortex rotates opposite to the main and corner vortices. The combined effect of these vortices distorts the temperature field in a channel and serves ultimately to bring about enhancement of heat transfer between the fluid and its neighboring surfaces. Higher heat transfer is usually accompanied by higher skin-friction coefficient. In order to be conclusive about the relative performance of the vortex generator for different angles of attack, the distribution of a quality factor (j/f) in the channel has been looked into. Thus, based on this analysis, and the enhancement of Nu_{sa}, the optimal choice of a vortex generator for a pre-assigned requirement can be prescribed.

Acknowledgements—One of the authors (GB) gratefully acknowledges the invitation and financial support from the Japan Society for the Promotion of Science (JSPS) for his stay with the Yokohama National University.

REFERENCES

1. R. L. Webb, Enhancement of single-phase convective heat transfer. In *Handbook of Single Phase Convective Heat Transfer* (Edited by S. Kakac, R. K. Shah and A. E. Bergles. Wiley, New York (1987).
2. C. M. B. Russel, T. V. Jones and G. H. Lee, Heat transfer enhancement using vortex generators, *Proceedings of the Seventh International Heat Transfer Conference*, Munich, Vol. 3, pp. 283–288 (1982).
3. M. Fiebig, P. Kallweit and N. K. Mitra, Wing type vortex generators for heat transfer enhancement, *Proceedings of the Eighth International Heat Transfer Conference*, San Francisco, Vol. 6, pp. 2909–2913 (1986).
4. M. Fiebig, P. Kallweit, N. K. Mitra and S. Tiggelbeck, Heat transfer enhancement and drag by longitudinal vortex generators in channel flow, *Expl Thermal Fluid Sci.* **4**, 103–114 (1991).
5. K. Torii, J. I. Yanagihara and Y. Nagai, Heat transfer enhancement by vortex generators, *Proceedings of the 3rd ASME/JSME Joint Thermal Engineering Conference*, Reno, Vol. III, pp. 1–7 (1991).
6. S. Tiggelbeck, N. K. Mitra and M. Fiebig, Flow structure and heat transfer in a channel with multiple longitudinal vortex-generators, *Expl Thermal Fluid Sci.* **5**, 425–436 (1992).
7. P. A. Eibeck and J. K. Eaton, Heat transfer effects of a longitudinal vortex embedded in a turbulent shear flow, *J. Heat Transfer* **109**, 16–24 (1987).
8. M. Fiebig, U. Brockmeier, N. K. Mitra and T. Güntermann, Structure of velocity and temperature fields in laminar channel flows with longitudinal vortex generators, *Numer. Heat Transfer A*, **15**, 281–302 (1989).
9. G. Biswas and H. Chattopadhyay, Heat transfer in a channel with built-in wing-type vortex generators, *Int. J. Heat Mass Transfer* **35**, 803–814 (1992).
10. G. Biswas, P. Deb and S. Biswas, Generation of longitudinal streamwise vortices—a device for improving

heat exchanger design, *J. Heat Transfer* **116,** 588–597 (1994).
11. K. Torii, K. Nishino and K. Nakayama, Mechanism of heat transfer augmentation by longitudinal vortices in a flat plate boundary layer, *Proceedings of the Tenth International Heat Transfer Conference*, Brighton, Vol. 6, pp. 123–128 (1994).
12. F. H. Harlow and J. E. Welch, Numerical calculation of time-dependent viscous incompressible flow of fluid with free surface, *Phys. Fluid* **8,** 2182–2188 (1965).
13. C. W. Hirt and J. L. Cook, Calculating three-dimensional flows around structures and over rough terrain, *J. Comput. Phys.* **10,** 324–340 (1972).
14. C. W. Hirt, B. D. Nichols and N. C. Romero, SOLA—a numerical solution algorithm for transient fluid flows, Los Alamos Scientific Laboratory Report, LA-5652 (1975).
15. R. K. Shah and A. L. London, *Laminar Flow Forced Convection in Ducts, Advances in Heat Transfer*, Suppl. 1, pp. 169–176. Academic Press, New York (1978).
16. JSME Data Book, *Flow Measurements*, pp. 118–119 (1985).